Monthly Notices of the ROYAL ASTRONOMICAL SOCIETY

MNRAS **530,** 3974–3985 (2024) https://doi.org/10.1093/mnras/stae1103
Advance Access publication 2024 April 24

Burst-induced spin variations in the accreting magnetic white dwarf PBC J0801.2–4625

Z. A. Irving [1]★ D. Altamirano,[1] S. Scaringi [2] M. Veresvarska [2] C. Knigge [1] N. Castro Segura,[1,3] D. De Martino[4] and K. Iłkiewicz[2,5]

[1]*School of Physics and Astronomy, University of Southampton, University Road, Southampton SO17 1BJ, UK*
[2]*Centre for Extragalactic Astronomy, Department of Physics, Durham University, South Road, Durham DH1 3LE, UK*
[3]*Department of Physics, University of Warwick, Gibbet Hill Road, Coventry CV4 7AL, UK*
[4]*INAF – Osservatorio Astronomico di Capodimonte, Salita Moiariello 16, I-80131 Napoli, Italy*
[5]*Astronomical Observatory, University of Warsaw, Al. Ujazdowskie 4, PL-00-478 Warszawa, Poland*

Accepted 2024 April 22. Received 2024 April 20; in original form 2024 March 2

ABSTRACT

PBC J0801.2–4625 is an intermediate polar with a primary spin frequency of 66.08 d^{-1} and an unknown orbital period. The long-term All Sky Automated Survey for Supernovae (ASAS-SN) light curve of this system reveals four bursts, all of which have similar peak amplitudes (∼2 mag) and durations (∼2 d). In this work, we primarily study the timing properties of this system's 2019 February burst, which was simultaneously observed by both ASAS-SN and the Transiting Exoplanet Survey Satellite (*TESS*). Pre-burst, a frequency of 4.064 ± 0.002 d^{-1}(5.906 ± 0.003 h period), likely attributed to the binary orbit, is identified in addition to previous measurements for the white dwarf's spin. During the burst, however, we find a spin frequency of 68.35 ± 0.28 d^{-1}. Post-burst, the spin returns to its pre-brust value but with a factor 1.82 ± 0.05 larger amplitude. The burst profile is double-peaked, and we estimate its energy to be 3.3×10^{39} erg. We conclude that the burst appears most consistent with thermonuclear runaway (i.e. a 'micronova'), and suggest that the spin variations may be an analogue to burst oscillations (i.e. 'micronova oscillations'). However, we also note that the above findings could be explained by a dwarf nova outburst. With the available data, we are unable to distinguish between these two scenarios.

Key words: stars: dwarf novae – stars: individual: PBC J0801.2–4625 – novae, cataclysmic variables.

1 INTRODUCTION

Dwarf novae (DNe) are cataclysmic variables (CVs) that undergo recurrent outbursts. CVs are binary systems containing a white dwarf (WD) primary and a low-mass secondary; Roche lobe overflow causes material to be stripped from the secondary and accreted onto the primary, typically via an accretion disc (Warner 1995). Patterson (1981) defines DN outbursts as ∼3–6 mag increases in brightness that occur every ∼1–6 months and return to quiescence in 3–20 d. DN outbursts can be explained by the disc instability model (DIM; see Lasota 2001 for a review), where instabilities develop in the accretion disc.

Typically, DN outbursts are observed in non-magnetic CVs, where the magnetic field of the WD primary is negligible. CVs with highly magnetized primaries are known as polars. In these systems, the magnetic field of the WD is $\gtrsim 10^7$ G (page 308 of Warner 1995), and its rotation period is synchronous with the orbital period of the system (known as sychronism); due to this synchronism, polars do not posses accretion discs. If, instead, the primary is only moderately magnetized, such that synchronism cannot be achieved, the system is referred to as an intermediate polar (IP; Warner 1995). IPs are particularly interesting due to their physical and observational similarities to low-mass X-ray binaries (LMXBs; e.g. Warner 1995, 2004).

In an IP, the WD may not have an accretion disc if its magnetic moment is particularly large (e.g. V2400 Ophiuchi; Buckley et al. 1995, 1997; Hellier & Beardmore 2002). However, many IPs do show signs of an accretion disc (e.g. Hellier 1991; Hellier, Garlick & Mason 1993; Parker, Norton & Mukai 2005). Since an accretion disc around a magnetized WD is truncated at the magnetospheric radius, infalling material travels along the magnetic field lines and is accreted on to the poles. Depending on the inclination, it is therefore possible to directly measure the spin of the WD in an IP. However, if such a system were to undergo a DN outburst, accretion may no longer be confined to the poles. In this case, pulsations at the spin frequency would not be observed, depending on the strength of the magnetic field (e.g. Hameury & Lasota 2017). Spin pulsations have been observed in the IPs GK Per and EX Hya during outburst in X-rays (e.g. Hellier et al. 2000; Zemko et al. 2017, repsectively), but similar pulsations are yet to be observed in the optical.

Within the DN outburst framework, the effect of a truncated accretion disc (as in IPs) is an increased recurrence time (e.g. Hameury & Lasota 2017). In addition, DN outbursts in magnetic CVs can also have shorter durations (e.g. Angelini & Verbunt 1989). Recently, however, it has been discovered that some very

★ E-mail: Z.Irving@soton.ac.uk

© The Author(s) 2024.
Published by Oxford University Press on behalf of Royal Astronomical Society. This is an Open Access article distributed under the terms of the Creative Commons Attribution-NonCommercial License (http://creativecommons.org/licenses/by-nc/4.0/), which permits non-commercial re-use, distribution, and reproduction in any medium, provided the original work is properly cited.

Downloaded from https://academic.oup.com/mnras/article/530/4/3974/7657819 by guest on 04 July 2024

short DN outbursts may be a result of localized thermonuclear runaways (TNRs; Scaringi et al. 2022b). Global TNRs are commonly observed in LMXBs, producing so-called Type-I X-ray bursts (see Galloway et al. 2008 for a review). In the framework of Scaringi et al. (2022a, b), material builds up on the poles of an accreting mildly magnetic WD until the pressure becomes sufficiently large to trigger a localized TNR, resulting in a 'micronova'. Micronovae are intrinsically interesting as nuclear phenomena, and the similarities to Type-I X-ray bursts further strengthen the link between LMXBs and magnetic CVs of the IP type.

Herein, we present an analysis of PBC J0801.2–4625's *TESS* Sector 8 (2019 February) light curve, during which the system underwent an eruption. PBC J0801.2–4625 is an IP with a primary spin frequency of 66.08 d^{-1} (Bernardini et al. 2017; Halpern et al. 2018) and an unknown orbital period. The *Gaia* parallax for this system is 0.704 ± 0.023 mas,[1] suggesting a geometric distance of 1355 ± 42 pc.[2] In Section 2, we discuss our data collection; in Section 3, we detail how we analysed these data; in Section 4, we present the results of this analysis; in Section 5, we attempt to provide physical interpretations for these results. We conclude that the burst's properties are most consistent with a micronova, though changes in the WD's spin pulsations are suggestive of changes in the accretion pressure, and thus a DN outburst. With the available data, we are unable to distinguish between burst mechanisms.

2 DATA

2.1 ASAS-SN

The All Sky Automated Survey for Supernovae (ASAS-SN) is a collection of ground-based optical observatories that monitors the entire visible sky. ASAS-SN has a nominal cadence of three observations per night (with each observation consisting of three dithered 90 s exposures), a limiting brightness of ∼17 mag, and 16 arcsec full width at half-maximum point spread function (Shappee et al. 2014; Kochanek et al. 2017). Early ASAS-SN observations used *V*-band filters, while the most recent observations use *g*-band filters. To extract a long-term ASAS-SN light curve for our source, we used the light-curve server,[3] which performs extractions using a two pixel (16 arcsec) aperture. PBC J0801.2–4625 has a *Gaia* proper motion of ∼2.5 mas yr^{-1}, which is negligible in the ∼7 yr ASAS-SN light curve.

2.2 *TESS*

In this work, we present data from the *Transiting Exoplanet Survey Satellite* (*TESS*), which can be obtained from the Mikilski Archive for Space Telescopes (MAST[4]). *TESS* is a spaced-based optical/near-infrared (600–1000 nm) all-sky survey telescope capable of producing science products with a cadence as high as 20 s. PBC J0801.2–4625 has been observed by *TESS* (Sector 8) between 2nd and 27th of February 2019 at 2-min cadence. To construct our light curve, we chose the SAP (simple aperture photometry) flux. The SAP flux was chosen in order to preserve all intrinsic variability of the source, which can be affected in the processed PDCSAP flux. The data were obtained using the `Lightkurve` Python package.[5] All data points with quality flag >0 have been removed to ensure minimal non-intrinsic contamination. To account for Barycentric corrections, we use *TESS*'s Barycentric Julian date.

3 METHOD

3.1 Cross-calibrating ASAS-SN and *TESS*

The light curves produced by *TESS* provide excellent relative photometry. To convert the *TESS* flux from electrons/s to mJy, and make use of absolute photometry, the *TESS* flux needs to be compared to nearly-simultaneous *ASAS-SN* *g*-band observations (e.g. Scaringi et al. 2022b). Comparing nearly simultaneous ASAS-SN and *TESS* observations, we can define a linear relationship:

$$F_{\mathrm{ASAS-SN}}\,[mJy] = A \times F_{\mathrm{TESS}}\left[e^{-}s^{-1}\right] + C, \tag{1}$$

where $F_{\mathrm{ASAS\text{-}SN}}$ and F_{TESS} are the ASAS-SN and *TESS* fluxes, respectively, and A and C are free parameters (Veresvarska et al. 2024). Converting the *TESS* flux from electrons/s to mJy therefore requires fitting for A and C on a case-by-case basis.

3.2 Detecting periodic signals

For detecting periodic signals, we use the Lomb–Scargle (L–S) periodogram (Lomb 1976; Scargle 1982).

3.2.1 *Problems of non-stationarity*

Detecting periodic signals in non-stationary time series (i.e. during a burst) is problematic for the L–S periodogram. To account for non-stationarity in our time series, we de-trend using a moving average with a window size of $5P_{\mathrm{spin}}$. This window size is large enough to have a minimal effect on the spin modulations, while also being small enough to remove the long-term variability.

3.2.2 *Normalization*

The power spectral density (PSD) normalized L–S periodogram (sometimes referred to as the unnormalized L–S periodogram) can be written as

$$P(f) = \frac{\chi^2_{\mathrm{const}} - \chi^2(f)}{2}, \tag{2}$$

where f is the frequency, and χ^2_{const} and $\chi^2(f)$ are the sum of the residuals around the best-fitting constant and periodic models, respectively (e.g. VanderPlas 2018). This normalization is particularly useful since, in the limit of evenly spaced data, it reproduces the standard Fourier power spectrum. In this work, we typically divide equation (2) by the root mean square (RMS) of the flux:

$$P_{\mathrm{RMS}}(f) = \frac{P(f)}{\mathrm{RMS}(\mathbf{y})}, \tag{3}$$

where $\mathbf{y}$ is the flux vector used to compute the L–S periodogram, to produce an RMS normalized power spectrum. The RMS normalized power has the same units as the flux, and its value is necessarily related to the RMS amplitude of the signal. The RMS normalized L–S periodogram is therefore better suited to comparing the relative amplitudes of signals.

[1] *Gaia* DR3 ID: 5518846852963401600.
[2] https://dc.zah.uni-heidelberg.de/gedr3dist/q/cone/form
[3] https://asas-sn.osu.edu/
[4] https://mast.stsci.edu/portal/Mashup/Clients/Mast/Portal.html
[5] https://docs.lightkurve.org/index.html

Downloaded from https://academic.oup.com/mnras/article/530/4/3974/7657819 by guest on 04 July 2024

3.2.3 *Frequency uncertainties*

To estimate the frequency uncertainties on features in our L–S periodograms, we re-sample the data points with replacement (as in Zurek et al. 2009). In doing this, a flux measurement F_i can only appear at time t_i, however, it can appear anywhere from 0 to N times (where N is the number of data points in the original light curve). This method therefore changes how each data point is weighted in the computation of the L–S periodogram, as well as slightly changing the window function. By taking the frequency of the tallest peak in the periodogram of each re-sampled light curve, we can construct a distribution of peak frequencies. This distribution will, in general, be multimodal, with modes corresponding to each (large) peak in the original light curve's periodogram. In our case, we found that these modes were well approximated as Gaussians, allowing us to describe the frequency of a given peak in the original light curve's periodogram as the mean ± the standard deviation of its corresponding mode.

3.3 Burst profile modelling

To fit and quantitatively compare burst models, we use nested sampling (Skilling 2004, 2009). We implement nested sampling using the MLFriends algorithm (Buchner 2016, 2019) via the `UltraNest`[6] package (Buchner 2021). Nested sampling is a Monte Carlo technique for computing the Bayesian evidence and constructing parameter posterior probability distributions. The Bayesian evidence is defined as

$$P(D|M) = Z = \int P(D|\theta, M)P(\theta|M)\mathrm{d}\theta, \tag{4}$$

where D represents some data, M represents some model, and θ represents some model parameters (e.g. Skilling 2004). $P(D|\theta, M)$ therefore represents the likelihood, and $P(\theta|M)$ represents the parameter prior probability distributions. The ratio of the Bayesian evidences between two models is known as the Bayes factor:

$$BF_{12} = \frac{Z_1}{Z_2}, \tag{5}$$

and this quantifies which model is more likely to have produced the observed data, assuming both models are equally probable a priori. $BF_{12} > 1$ indicates a preference for model 1, while $BF_{12} < 1$ indicates a preference for model 2. Buchner et al. (2014) showed that false decision rates lower than 1 per cent can be achieved using a threshold of $BF_{12} = 10$; as such, we consider $BF_{12} \geq 10$ to constitute a significant preference for model 1 over model 2. In cases where the Bayes factor is not significant, simulations can be used to determine a corresponding false decision rate, as in Buchner et al. (2014).

To fit our models, we use a simple Gaussian likelihood:

$$\mathcal{L} = -\frac{1}{2}\sum\left(\frac{F_{\mathrm{obs}} - F_{\mathrm{model}}}{\sigma}\right)^2, \tag{6}$$

where F_{obs} are the observed fluxes, F_{model} are the model fluxes, and σ are the errors on the observed fluxes. For our burst shape, we consider two simple models. The first model is an asymmetric/skewed Gaussian function:

$$F_{\mathrm{skewed\ Gauss}}(t) = \begin{cases} A\exp\left(-\frac{(t-\mu)^2}{2\sigma_{\mathrm{rise}}^2}\right) + o & \text{if } t \leq \mu \\ A\exp\left(-\frac{(t-\mu)^2}{2\sigma_{\mathrm{decay}}^2}\right) + o & \text{otherwise} \end{cases}, \tag{7}$$

[6]https://johannesbuchner.github.io/UltraNest/

Table 1. Prior probability distributions for our model parameters.

Parameter	Prior
A, B	$log\mathcal{U}(min(ferr), 10(max(f) - min(f)))$
μ	$\mathcal{U}(min(t), max(t))$
$\sigma_{\mathrm{rise}}, \sigma_{\mathrm{decay}}, \tau$	$log\mathcal{U}(min(\delta t), max(t) - min(t))$
o	$\mathcal{U}(min(f), max(f))$

Notes. $\mathcal{U}(a, b)$ represents a prior that is uniform from a to b, while $log\mathcal{U}(a, b)$ denotes a prior that is uniform in logarithm. f represents the flux measurements, $ferr$ represents the errors on these measurements, t represents the observation time, and δt represents the observing cadence.

where t represents time, A is the amplitude, μ is the time of flux maximum, σ_{rise} and σ_{decay} are related to the rise and decay timescales, respectively, and o is the quiescent emission level. When fitting this model, we impose the constraint that σ_{rise} must be less than σ_{decay} to mimic the fast-rise-exponential-decay characteristic typical of astrophysical burst events. The second model we consider is a superposition of two skewed Gaussian functions; when fitting this model, we further imposed the constraint that μ_1 must be less than μ_2 to avoid overlapping bursts and degeneracies in the parameter space. We present the priors for each of our model parameters in Table 1.

To compute the Bayesian evidence for our two burst models, we use `UltraNest`'s `SliceSampler` step sampler. We prefer a step sampler in this case since we found that `UltraNest`'s default sampler resulted in low sampling efficiency, and thus required long compute times to reach convergence. When using a step sampler, the sampling efficiency is inversely proportional to the number of steps, allowing steady progress to be made in even the most tricky of cases. To use a step sampler, two parameters must be defined: the number of steps and the direction proposal algorithm. Buchner (2022) compared 10 different direction proposal algorithms and found that, in general, their 'de-mix' algorithm performed the best. 'de-mix' randomly chooses between whitened slice sampling and differential evolution with equal probability (see Buchner 2022 for more details on these algorithms). They also found that this direction proposal algorithm requires at least two steps per dimension (i.e. two steps per model parameter) to avoid biases. For these reasons, we use the 'de-mix' direction proposal algorithm (implemented in `UltraNest` via the `generate_mixture_random_direction` function) with two steps per model parameter. To ensure our results are robust against step sampler biases, we re-run our samplers and double the number of steps each time until the results from consecutive runs are within error.

4 RESULTS

4.1 Long-term ASAS-SN light curve

In Fig. 1, we present the long-term ASAS-SN light curve for PBC J0801.2–4625. This light curve shows an average flux of ∼ 15–16 mag, with a slowly decreasing global trend. We identify four burst events with vertical dashed lines labelled 1–4 chronologically. Bursts are separated by ∼ 1–2 yr, and show similar peak amplitudes of ∼2 mag and durations of ≲ 2 d. However, further bursts may have been missed due to ASAS-SN's observing cadence, or if they occurred between observing seasons. At the time of writing, only one burst (burst 2) has been observed simultaneously by both ASAS-SN and *TESS*.

Downloaded from https://academic.oup.com/mnras/article/530/4/3974/7657819 by guest on 04 July 2024

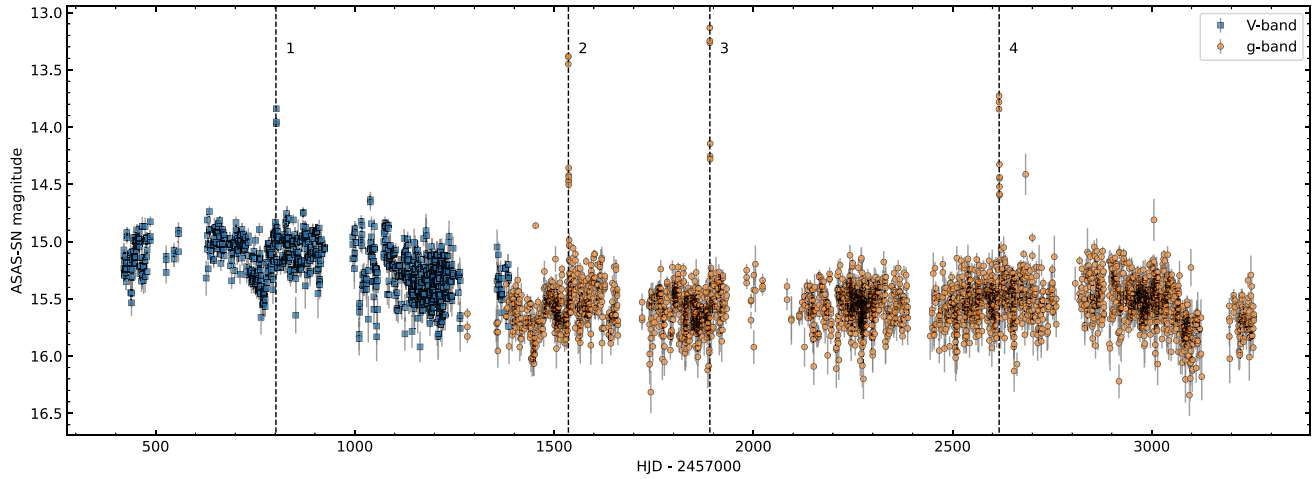

Figure 1. ASAS-SN light curve of PBC J0801.2–4625. ASAS-SN has a nominal cadence of three observations per night. The data points are colour-coded by filter (legend), and the dashed lines identify four burst events numbered 1–4 chronologically.

4.2 Cross-calibration

In Fig. 2, we present the cross-calibrated ASAS-SN and *TESS* Sector 8 light curve, with a zoomed inset corresponding to the shaded grey region. No bolometric correction has been applied to account for any potential differences in bolometric correction during the burst and in quiescence. For the first half of Sector 8, the calibration parameters are $A = 0.017 \pm 0.001 \frac{mJy}{e^{-}s^{-1}}$ and $C = -4.0 \pm 0.5$ mJy (equation 1). Similarly, for the second half the parameters are $A = 0.0239 \pm 0.0003 \frac{mJy}{e^{-}s^{-1}}$ and $C = -7.2 \pm 0.1$ mJy. This figure shows that the rise time of the burst is $\leq$0.5 d, and the addition of the *TESS* data reveals a slightly larger peak amplitude than that suggested by Fig. 1. That said, *TESS* may have missed the peak of the burst as its onset coincides with a gap in the higher cadence data; for this reason, we refer to the *TESS* data before the gap (i.e. before BJD 2458530) as the pre-burst segment, and the data after the gap as the burst + post-burst segment.

4.2.1 *Comparing single- and double-peaked burst shapes*

Fig. 2 appears to show a secondary peak during the decay of the burst at BJD ∼2458536. To verify the significance of this secondary peak, we compared single- and double-peaked burst models as described in Section 3.3. To estimate the errors on our *TESS* flux measurements, we assumed Poisson statistics. However, *TESS* data are not strictly Poissonian after background corrections, and so these errors are overestimated. For the purposes of modelling the burst, however, the effects of this error overestimation are minimal.

Comparing the Bayesian evidences for the single- and double-peaked burst models, the Bayes factor is $e^{14145.96 \pm 0.85}$ in favour of the double-peaked model. This value is well in excess of our significance threshold, and so we choose not to calibrate this value to a false decision rate. The resulting burst shape is shown in Fig. 3.

4.3 Pre-burst

In Fig. 4, we present a PSD normalized L–S periodogram of Fig. 2's pre-burst *TESS* data. To produce this periodogram, we fit for the mean of the data (i.e. we computed a 'floating-mean periodogram'; Cumming, Marcy & Butler 1999; VanderPlas & Ivezić 2015), and use the full frequency range: $1/T$–$1/2\delta t$ (∼0.1–360.0 d^{-1}), where T is the time span of the observation (∼ 11 d) and δt is the observing cadence (2 min). The resulting periodogram shows red noise at low frequencies, while white (Poisson) noise dominates at high frequencies. We identify three prominent features in this periodogram at frequencies of ∼4, ∼66, and ∼132 d^{-1} using vertical lines.

In Fig. 5, we present a dynamical power spectrum of Fig. 2's pre-burst *TESS* data after de-trending. To compute this dynamical spectrum, 1 d segments were used with offsets of one data point to allow for maximum overlap. The powers have been RMS normalized, and the frequency range corresponds to ±10 per cent of the expected spin frequency (∼66 d^{-1}; Halpern et al. 2018). The contours represent the relative powers of features in the spectrum, and the time at which each underlying L–S periodogram appears in the dynamical spectrum corresponds to the mean time of the epoch used to compute the periodogram (see e.g. Watts 2012 for more details on dynamical power spectra). This figure reveals no significant evolution in the frequency of the signal, though there is some variation in the peak power. The maximum in the peak power occurs at BJD ∼2458520.2, while the minimum occurs approximately 1.5 d later. The maximum and minimum peak powers correspond to frequencies of 66.04 and 66.12 d^{-1}, respectively, the ratio between their powers is 3.05, and the ratio between the corresponding RMS fluxes (before de-trending) is 1.13. We note that cycle-to-cycle amplitude variations are common in IPs and magnetic CVs more generally (e.g. O'Donoghue, Koen & Kilkenny 1996; Reimer et al. 2008).

4.4 Burst + post-burst

In Fig. 6, we show L–S periodograms from three different epochs. When computing these periodograms, the light curves were de-trended and the powers were RMS normalized. The spin frequency of the WD (66.08 d^{-1}; Halpern et al. 2018) is shown by the solid vertical line in each periodogram. The periodograms of the first and last epochs show a single prominent feature at the WD spin frequency. However, the periodogram of the middle epoch has its most prominent feature at a decidedly higher frequency, and a less prominent feature close to, but slightly above, the WD spin frequency. We also note that the powers of these features are all considerably different: The periodogram of the last epoch has the greatest peak

Downloaded from https://academic.oup.com/mnras/article/530/4/3974/7657819 by guest on 04 July 2024

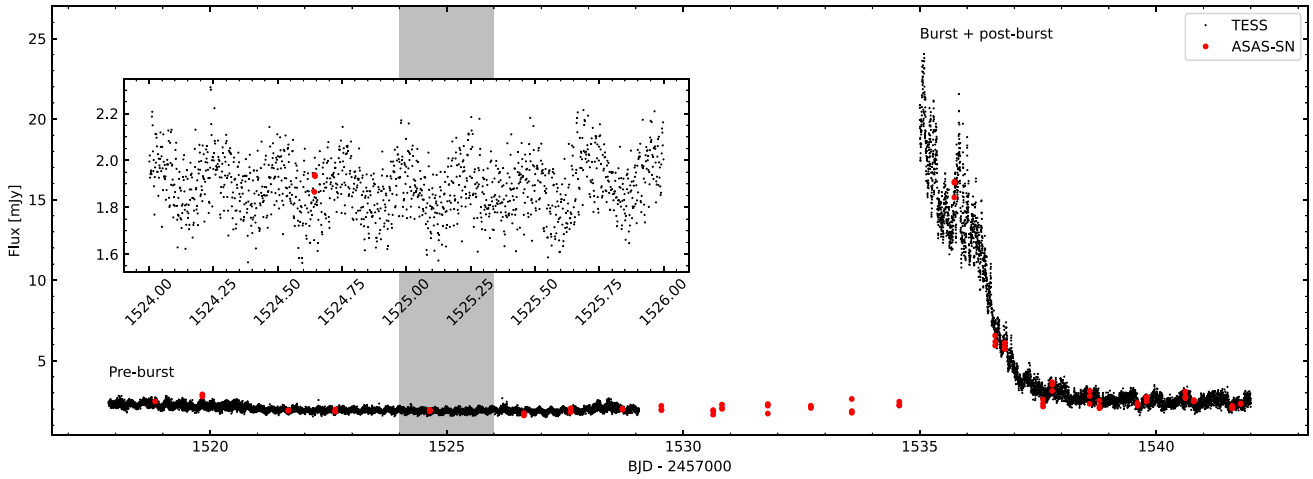

Figure 2. Cross-calibrated light curve of PBC J0801.2–4625. The red o markers show the ASAS-SN data, while the black point markers show the *TESS* Sector 8 data at 2-min cadence. The inset shows a zoomed section of the quiescent emission indicated by the shaded grey region. Since the gap in these data coincides with a burst event, we refer to the data before the gap as the pre-burst segment, and the data after the gap as the burst + post-burst segment.

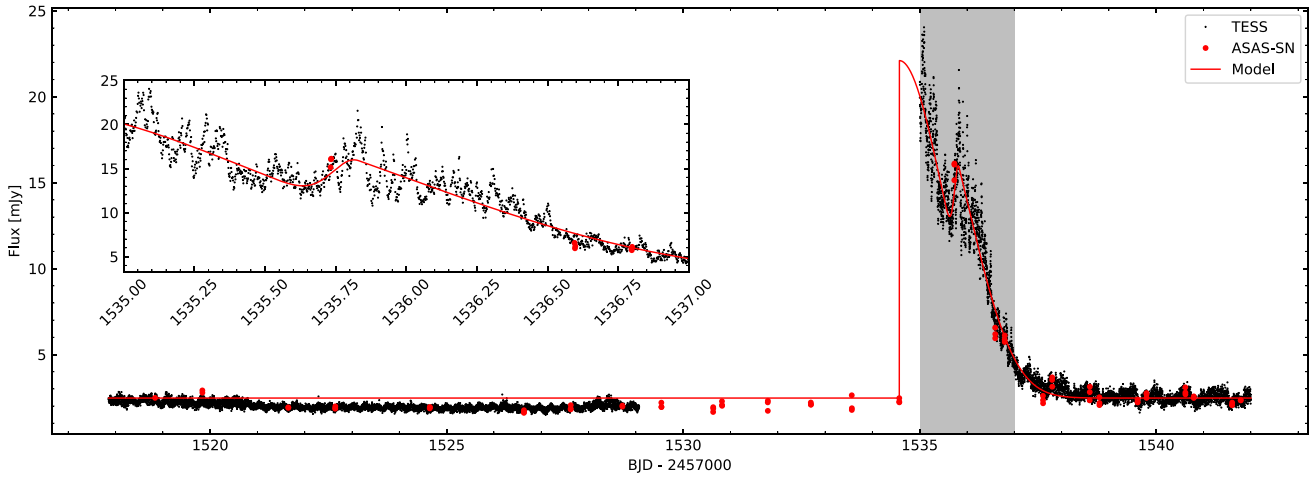

Figure 3. Fig.2 with best-fitting burst model (red line). The zoomed inset shows the second peak in the burst and corresponds to the shaded grey region.

power, followed by the periodogram of the first epoch (a factor 2.3 lower), with the periodogram from the middle epoch having the lowest peak power (a factor 3.1 lower than the peak power of the final epoch).

In Fig. 7, we present L–S periodograms and bootstrapped frequency distributions corresponding to different sections of the burst + post-burst *TESS* data of Fig. 2. As in Fig. 6, the light curves were de-trended and the powers are RMS normalized. The spin frequency of the WD (66.08 d^{-1}; Halpern et al. 2018) is shown by the solid vertical line in each periodogram. This figure shows how the signal around the known spin frequency of the WD evolves during the burst: In the first epoch, the most prominent feature in the L–S periodogram is significantly higher than the WD spin; this higher frequency signal gets superseded later in the burst by a signal slightly above the WD spin frequency (second epoch); later still (third epoch), the two frequencies from the second epoch appear to merge into a single feature somewhat above the WD spin frequency; after approximately 2 d (final two epochs), the signal returns to being consistent with the known spin frequency of the WD. Fig. 7 also shows that the amplitudes of the aforementioned signals vary considerably on timescales <1 d.

In Fig. 8, we present a dynamical power spectrum of the burst + post-burst *TESS* data from Fig. 2 after de-trending. This dynamical power spectrum was computed, and is presented, in the same way as Fig. 5. In contrast to Fig. 5, this figure shows significant evolution in the frequency of the signal, in addition to variations in the peak power. Similarly to Figs 6 and 7, Fig. 8 shows features above the WD spin frequency drifting downward, asymptoting at the WD spin (dashed black line). Interestingly, this figure shows that the peak power reaches a maximum at BJD ∼24571537.7, where the peak power is a factor 1.6 larger than the peak power at the end of the spectrum. The frequency at which this dynamical power spectrum achieves its maximum peak power is 66.11 d^{-1}, consistent with the 66.08 d^{-1} peak from Fig. 4. We emphasize, however, that due to how this dynamical power spectrum has been computed, changes in frequency may appear artificially smoothed, and so we caution against misinterpreting this figure.

Downloaded from https://academic.oup.com/mnras/article/530/4/3974/7657819 by guest on 04 July 2024

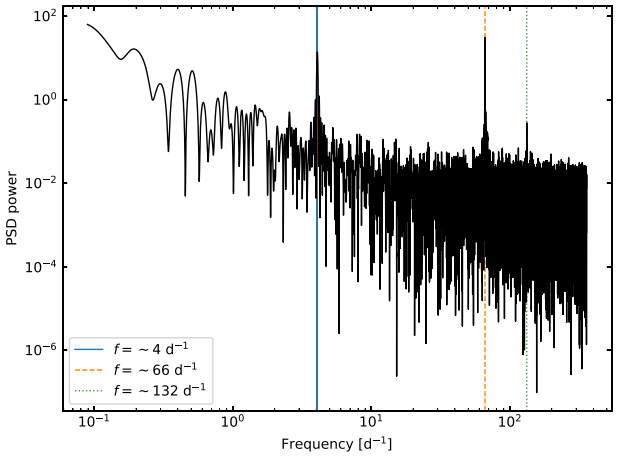

Figure 4. PSD normalized L–S periodogram of Fig. 2's pre-burst *TESS* data. Three prominent features in the periodogram are identified at frequencies of ∼4, ∼66, and ∼132 d^{-1}. We note the presence of red noise at low frequencies, while high-frequency powers appear to show primarily white noise.

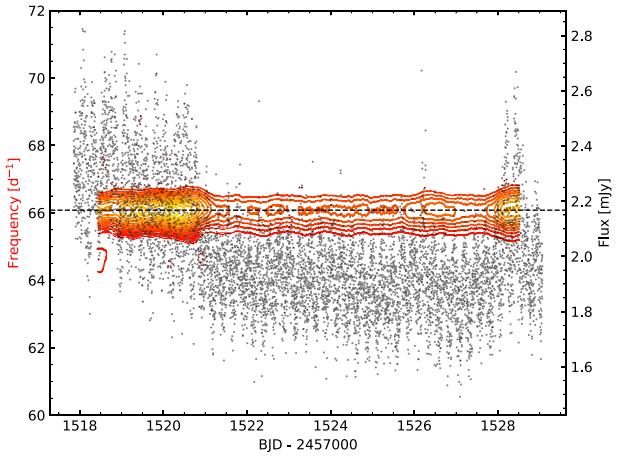

Figure 5. Dynamical power spectrum of the de-trended pre-burst light curve atop the pre-burst light curve. To compute this dynamical spectrum, 1-d segments were used; between successive periodograms, the segment window was shifted by one data point to allow for maximum overlap. The powers have been RMS normalized, and the frequency range corresponds to ±10 per cent of the expected spin frequency (66.08 d^{-1}; dashed black line). The time at which each underlying L–S periodogram appears in the dynamical spectrum corresponds to the mean time of the epoch used to compute the periodogram.

Finally, in Fig. 9, we present a second dynamical power spectrum of the burst + post-burst *TESS* data from Fig. 2 after de-trending. This dynamical power spectrum was computed, and is presented, in a similar way to Fig. 5, however, the frequency range now corresponds to ±10 per cent of the twice the WD spin (i.e. 132.15 d^{-1}). In contrast to Fig. 8, Fig. 9 shows an upward frequency drift with a peak in the RMS amplitude of the signal occurring at BJD ∼2458539 d. However, it is also clear that during the burst the harmonic's statistics are quite poor, as evidenced by the numerous additional contours at unassociated frequencies. Therefore, while we include this result here, we primarily focus on the fundamental frequency since its statistics are better.

5 DISCUSSION

In Section 4, we showed that PBC J0801.2–4625's long-term ASAS-SN light curve (Fig. 1) shows four bursts separated by ∼ 1–2 yr. All four bursts have comparable peak amplitudes (∼ 1–2 mag) and durations (≲ 2 d), and the second burst identified in this figure was simultaneously observed by *TESS* (Fig. 2). Using the high-cadence *TESS* data, we showed that there are significant changes in the power spectrum around the WD spin frequency during the burst (Figs 6–8). Below, we attempt interpret these results.

5.1 Long-term ASAS-SN light curve

It is clear from Fig. 1 that burst 2, which occurred in 2019 February and was simultaneously observed by *TESS*, does not appear atypical: It has an unremarkable peak amplitude and duration relative to the other bursts. We therefore assume that Fig. 2 is representative of PBC J0801.2–4625's typical bursting behaviour.

5.2 Pre-burst

5.2.1 Orbit

The spin frequency of PBC J0801.2–4625's WD is known to be 66.08 d^{-1} (Bernardini et al. 2017; Halpern et al. 2018), so the low-frequency feature at ∼4 d^{-1} ($P \approx 6$ h) in Fig. 4 is unlikely to be associated with the WD spin. However, a number of CVs have orbital periods, $P_{\rm orb}$, of approximately 6 h, for example: AH Eridani ($P_{\rm orb} = 5.74$ h; Thorstensen 1997), Nova Aquilae 1995 ($P_{\rm orb} = 6.14$ h; Retter, Leibowitz & Kovo-Kariti 1998), TX Columbae ($P_{\rm orb} = 5.69$ h; Buckley & Tuohy 1989; Rawat, Pandey & Joshi 2021), and XY Arietis ($P_{\rm orb} = 6.06$ h; Allan, Hellier & Ramseyer 1996). We therefore attribute the feature at ∼4 d^{-1} to the orbital frequency of this system. By bootstrapping the light curve, we find an orbital period of 5.906 ± 0.003 h. To our knowledge, this is the first time the orbital period of this system has been reported.

5.2.2 WD Spin

Since the spin frequency of PBC J0801.2–4625's WD is known to be 66.08 d^{-1} (Halpern et al. 2018), we attribute the feature at ∼66 d^{-1} in Fig. 4 to the spin frequency of the WD. Bootstrapping the light curve yields a spin frequency of 66.081 ± 0.001 d^{-1}, corresponding to a period of 21.7916 ± 0.0004 min.

5.3 Burst energy

With the source distance, and *TESS*'s filter width (500 nm; Section 2.2), we can convert the burst model (Fig. 3) from spectral flux density to luminosity. By then integrating the luminosity model, and subtracting the quiescent emission, we estimate the total energy emitted during the burst to be 3.3×10^{39} erg. However, that our luminosity is likely underestimated for two reasons: (i) we have not accounted for any bolometric correction when cross-calibrating ASAS-SN and *TESS*, (ii) we assume a flat emission spectrum when converting from spectral flux density to luminosity. As such, our burst energy is also likely underestimated.

Downloaded from https://academic.oup.com/mnras/article/530/4/3974/7657819 by guest on 04 July 2024

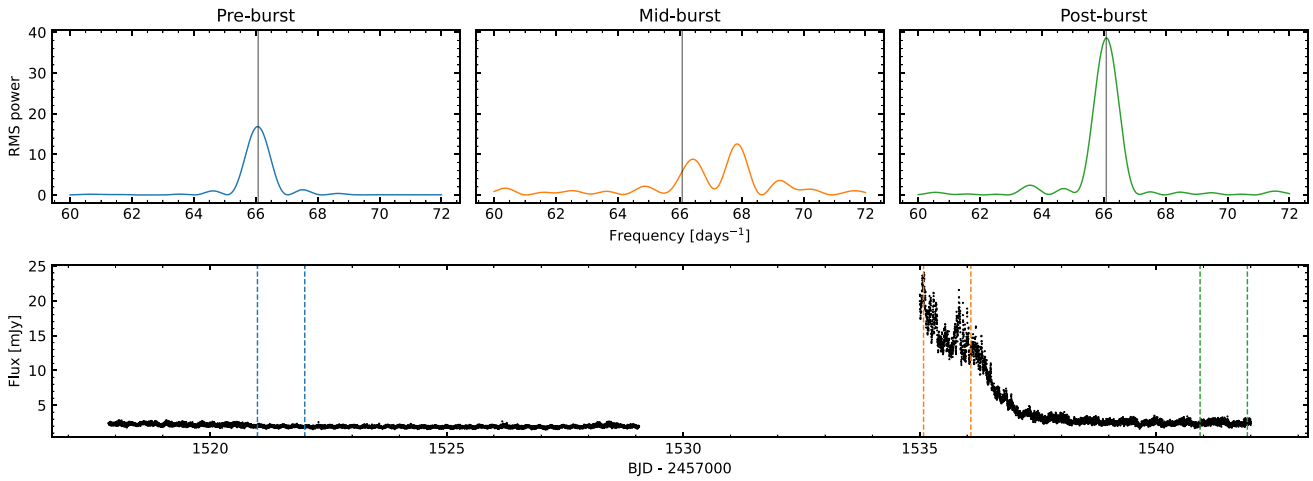

Figure 6. Top panel: L–S periodograms computed from non-overlapping segments of the light curve shown in the bottom panel. The black vertical lines in the top panel show the spin frequency of the primary (66.08 d^{-1}). The periodograms are colour-coded to match the windows highlighted by the vertical dashed lines in the bottom panel.

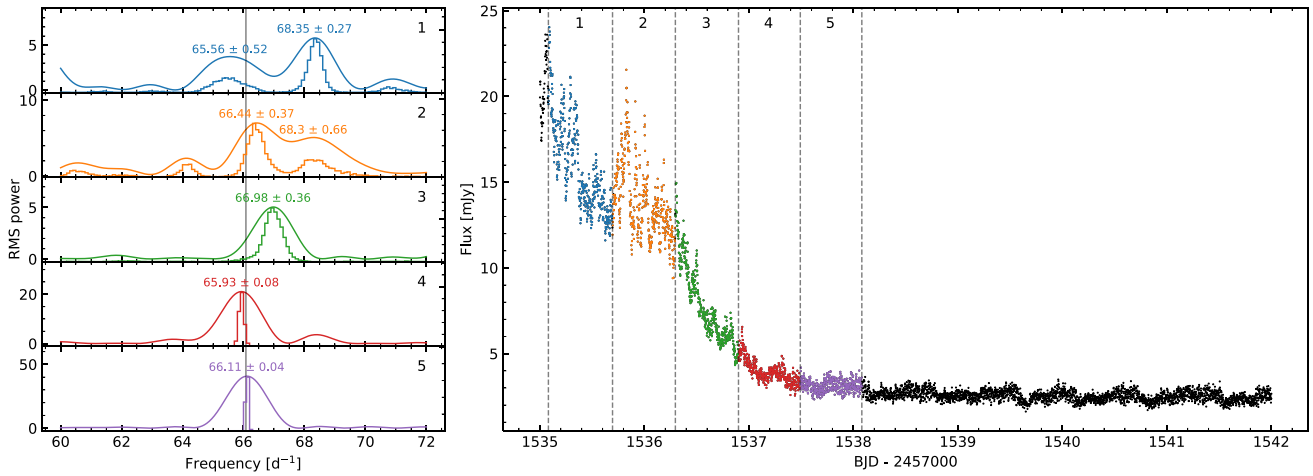

Figure 7. L–S periodograms and bootstrapped frequency distributions (left panel) for corresponding epochs in the second half of the *TESS* Sector 8 light curve (right panel).

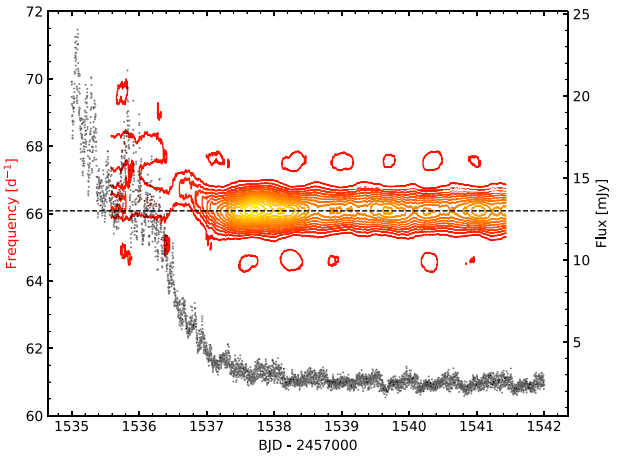

Figure 8. Similar to Fig. 5, but for the burst + post-burst segment of Fig. 2.

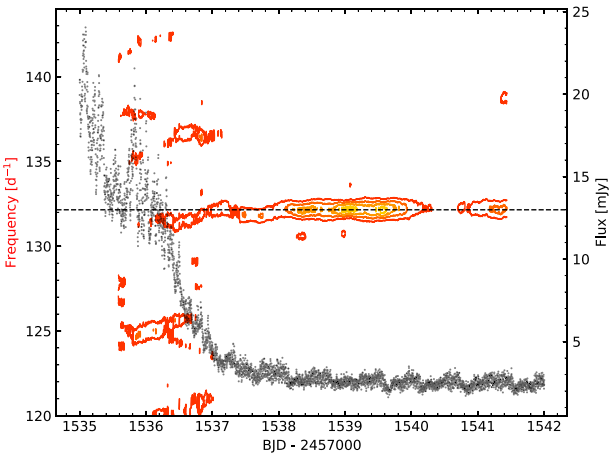

Figure 9. Similar to Fig. 8, but showing the first harmonic of the WD spin.

Downloaded from https://academic.oup.com/mnras/article/530/4/3974/7657819 by guest on 04 July 2024

5.4 Burst mechanisms

5.4.1 Micronovae

The burst energy from Section 5.3 is remarkably consistent with the energy emitted during a micronova (Scaringi et al. 2022b). Below, we therefore consider whether our results can be interpreted within the micronova framework.

Scaringi et al. (2022b) analyse burst events from three accreting WD systems: TV Columbae (TV Col), EI Ursae Majoris (EI UMa), and ASASSN-19bh. The light curves of TV Col and EI UMa show consecutive short (< 1 d) bursts, while the light curve for ASASSN-19bh shows a single, extended (> 1 d) burst. ASASSN-19bh has a simple burst shape compared to TV Col and EI UMa. Scaringi et al. (2022b) calculate burst energies of 3.5×10^{38}, 5.2×10^{38}, and 1.2×10^{39} erg for TV Col, EI UMa, and ASASSN-19bh, respectively.[7] In the context of Scaringi et al. (2022b), we note that Fig. 3 is most similar to the burst of ASASSN-19bh (their fig. 2). However, the most striking similarity can be seen when comparing Fig. 3 to a number of Type-I X-ray bursts, for example: 4U 1636–535 (Bhattacharyya & Strohmayer 2006a), 4U 1608–52 (Jaisawal et al. 2019), and SAX J1808.4–3658 (Bult et al. 2019).

To explain double-peaked Type-I X-ray bursts, Bhattacharyya & Strohmayer (2006b) suggested a stalling of the TNR, though the underlying physical mechanism responsible for this is unclear. Jaisawal et al. (2019) concluded that the double-peaked burst shape of 4U 1608-52 was most likely due to the reburning of fresh or leftover material during the cooling tail (Keek & Heger 2017). Interestingly, Jaisawal et al. (2019) also noted that if matter is confined to a small region, two bursts occurring nearly simultaneously could produce a burst that appeared double-peaked. However, Jaisawal et al. (2019) concluded that two nearly-simultaneous bursts was unlikely in their case since 4U 1608-52's magnetic field is too weak.

Assuming the burst presented in Fig. 3 is indeed a micronova, we find two compelling explanations for the double-peaked shape: (i) the first peak is a standard micronova (Scaringi et al. 2022a, b) and the second peak is due to the reburning of fresh or leftover material (Keek & Heger 2017; Jaisawal et al. 2019), (ii) the two peaks are separate micronovae on opposite hemispheres that occur nearly simultaneously. We find (i) to be more likely since (ii) would require almost identical accretion rates on to the poles and extremely similar accretion column fractional areas (Scaringi et al. 2022a, b).

Regarding the recurrence times of micronovae, Scaringi et al. (2022a) show that

$$t_{\rm rec} = \frac{M_{\rm col}}{\dot{M}_{\rm acc}}, \tag{8}$$

where $t_{\rm rec}$ is the recurrence time, $M_{\rm col}$ is the accretion column mass, and $\dot{M}_{\rm acc}$ is the accretion rate. Scaringi et al. (2022a) note that typical mass-transfer rates of $10^{-10}\,{\rm M}_{\odot}\,{\rm yr}^{-1}$ can trigger micronovae with a recurrence time of $t_{\rm rec} \approx 100$ d. Fig. 1 suggests an upper limit on the recurrence time of $\sim$ 1–2 yr, a factor $\sim$ 3.7–7.3 larger than the recurrence time for a typical accretion rate; this may be suggestive of PBC J0801.2–4625 having a below-average accretion rate for its 5.9 h orbital period (following the $\dot{M}_{\rm acc}$–$P_{\rm orb}$ relation of Knigge, Baraffe & Patterson 2011). Alternatively, PBC J0801.2–4625 may have a more typical accretion rate for its orbital period ($\dot{M}_{\rm acc} \sim 10^{-9}{\rm M}_{\odot}$ yr^{-1} according to Knigge et al. 2011), but not all of this accreted material is confined to the poles. That said, we note that the calibrations of Knigge et al. (2011) are only appropriate for unevolved CV donors, which may not be the case for PBC J0801.2–4625 given its 5.9 h orbital period.

[7]Note: The energies for TV Col and EI UMa are summed over their consecutive bursts.

5.4.2 Dwarf nova outburst

The burst frequency suggested by Fig. 1 is consistent with DN outbursts in an IP (e.g. Hellier et al. 2000), as are the amplitude and duration of the burst shown in Fig. 3. For these reasons, it is difficult to dismiss the possibility that PBC J0801.2–4625 exhibits DN outbursts and not micronovae.

Hameury & Lasota (2017) investigate DN outburst mechanisms in IPs, and show that the DIM can only explain long (i.e. a few days) outbursts in such systems. For shorter outbursts, enhanced mass transfer or, more likely, an instability coupling the WD magnetic field with that generated by the magnetorotational instability operating in the accretion disc is needed. In our case, the burst duration shown in Fig. 3 ($\sim$2 d) is between the long and short regimes, meaning we cannot confidently distinguish between DN outburst mechanisms.

Following a DN outburst, 'rebrightenings' are sometimes observed (e.g. Hameury & Lasota 2021). However, these rebrightenings are typically observed in WZ Sge stars, where the outburst peak amplitude is large ($\sim$8 mag) and the recurrence time is long [$\mathcal{O}$(decades)] (e.g. Kato 2015). Fig. 1 shows recurrence times $\mathcal{O}$(years), too short for a WZ Sge star, and further shows no evidence for rebrightenings following any of the observed bursts. As such, interpretation of Fig. 3's double-peaked shape within the DN outburst framework is difficult.

5.4.3 Classification

Having considered PBC J0801.2–4625's bursts within the micronova and DN outburst frameworks in Sections 5.4.1 and 5.4.2, respectively, we favour the micronovae interpretation. We find the qualitative similarities between Fig. 3 and a number of Type I X-ray bursts particularly compelling, in addition to the similar burst energy to ASASSN-19bh's micronova in Scaringi et al. (2022b). To classify the burst mechanism more quantitatively, however, Iłkiewicz et al. (2024) showed that burst events in CVs can be classified using a series of 'diagnostic diagrams'. To make use these diagnostic diagrams, we use the peak spectral flux density of the model shown in Fig. 3 to infer a peak luminosity of $\sim 2.9 \times 10^{34}\,{\rm erg\,s^{-1}}$ (recalling that this luminosity is likely underestimated for the reasons outlined in Section 5.3). Assuming a burst duration of 2 d (lower limit of Fig. 3), and using the burst energy from Section 5.3, it is clear that PBC J0801.2–4625's 2019 February burst is most consistent with a micronova. Indeed, DN outbursts typically have peak luminosities and total energies approximately an order of magnitude lower than our inferred values (Iłkiewicz et al. 2024).

5.5 Burst + post-burst

5.5.1 Validating the change in frequency during the burst

Figs 6–8 all suggest a change in the spin pulsations of PBC J0801.2–4625's WD during its 2019 February burst. However, since these figures only show a narrow frequency range around the spin, it is unclear whether there are more prominent features outside of this range. In Fig. 10, we therefore present an L–S periodogram of the first day of the de-trended burst + post-burst segment of Fig. 2 (i.e. the 'mid-burst' epoch from Fig. 6) using the full frequency range: $1/T$–$1/2\delta t$ (1.0–360.0 d^{-1}).

Downloaded from https://academic.oup.com/mnras/article/530/4/3974/7657819 by guest on 04 July 2024

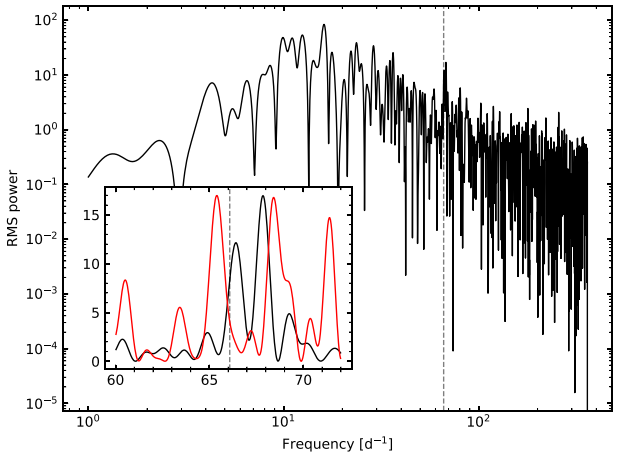

Figure 10. L–S periodogram of the first day of the (de-trended) burst + post-burst segment of Fig. 2 (black) and the corresponding window function (red, arbitrarily scaled). The vertical dashed line shows the spin frequency of the WD (66.081 d^{-1}). The inset shows a zoomed section of the power spectrum at ±10 per cent of the WD spin. The bend in the periodogram at ∼15 d^{-1} results from de-trending the light curve: we de-trended using a moving average with a window size of $5P_{\rm spin}$ (Section 3.2.1), which corresponds to a frequency of 13.2 d^{-1}.

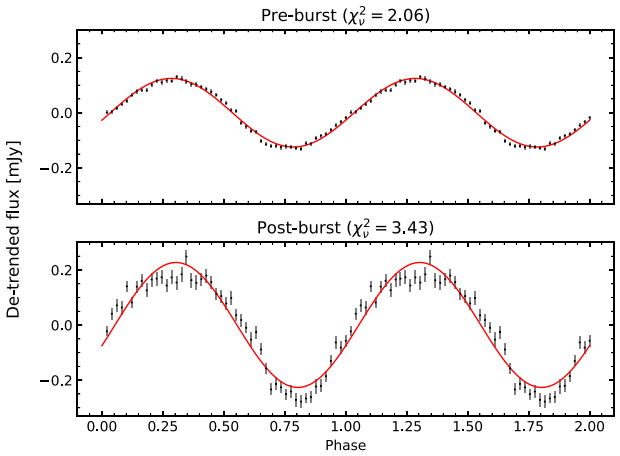

Figure 11. Phase binned Fig. 2 after de-trending. The red lines show the best-fitting sinusoids for each light curve. Both light curves were folded on the spin frequency of the primary (66.081 d^{-1}). When folding the burst + post-burst light curve, all data before BJD 2458538 d were excluded. The error bars show the standard error on the binned fluxes, and the reduced chi-squared, χ^2_ν, values for the sinusoid models are given in the panel titles.

From Fig. 10, it is clear to see that the features shown in the mid-burst epoch of Fig. 6 are the only prominent features in the power spectrum (not including the power-law noise). Moreover, it is also clear that the window function cannot be producing both of the prominent peaks since the frequencies and spacing between features in the window function do not align with the features in the power spectrum. Moreover, the frequency change is not due to a spin–orbit sideband. As discussed in Section 5.2.1, the orbital frequency of this system is 4.08 d^{-1}; a sideband would therefore result in a peak at 66.08 ± 4.08 d^{-1}, which is not what we find. Therefore, we conclude that the apparent change in the spin pulsations is real.

To rule out the possibility that our de-trending method is the cause of the frequency change seen in Figs 6–8, we also de-trend the burst using a parametric function instead of a moving average. Since we are only interested in the burst + post-burst segment of Fig. 2, instead of fitting two asymmetric Gaussian functions, as in Section 4.2.1, we fit a skewed Gaussian + exponential decay function:

$$F(t) = F_{\rm skewed\ Gauss}(t) + B\exp\left(\frac{t-t_0}{\tau}\right), \quad (9)$$

where B and τ are the amplitude and decay time-scale of the exponential component, respectively, and t_0 is the time of the first observation (which acts to relax the definition of the amplitude). We prefer this model when fitting the burst + post-burst segment of Fig. 2 since the parameters for two skewed Gaussians become poorly constrained when the pre-burst segment is omitted. We then fit this model in the same way described in Section 3.3, noting that here we are only interested in fitting the model, not comparing it. The priors for equation (9)'s parameters are given in Table 1. After de-trending the burst in this way, we reproduce the same frequency change discussed above.

5.5.2 *Spin pulsation amplitude*

In Fig. 11, we present the results of phase binning both segments of Fig. 2 on the WD spin frequency (66.081 d^{-1}). When phase binning the burst + post-burst segment of Fig. 2, all data before BJD 2458538 d were excluded.

As can be seen in Fig. 11, the average amplitude of the spin pulsations after the burst is larger than before the burst. Using the sinusoid models shown in the figure, and assuming negligible background contributions, the amplitude of the spin pulsations increases by a factor 1.82 ± 0.05. Before the burst, the peak-to-peak RMS amplitude of the spin pulsations is 12.3 ± 0.1 per cent, while after the burst it is 17.7 ± 0.5 per cent.

The reduced chi-squared, χ^2_ν, values in Fig. 11 show that the spin pulsations appear less sinusoidal following the burst, suggesting an increase in the amplitude of the first harmonic of the spin. Performing the same analysis as described above, but for the spin's first harmonic ($f_{\rm harmonic}$ = 132.15 cyc d^{-1}), we find that the average RMS amplitude of the harmonic increases by a factor 4.1 ± 0.5. The peak-to-peak RMS amplitude of the harmonic is 1.1 ± 0.1 per cent before the burst, but 3.7 ± 0.3 per cent following the burst. The χ^2_ν values are 0.72 and 0.65 for the pre- and post-burst segments, respectively.

5.6 Relating the change in frequency to the micronova scenario

In Section 5.5, we established that the change in the apparent spin frequency during the burst, seen in Figs 6–8, is real. Below, we attempt to interpret this within the context of a micronova by making analogies to LMXBs.

5.6.1 *An analogue to type I X-ray burst oscillations? Micronova oscillations?*

Burst oscillations (BOs) are a well-documented phenomena in Type I X-ray bursts (see Watts 2012 for a review). Notable characteristics of BOs include: an upward frequency drift during the rise of the burst, a low RMS amplitude during the peak of the burst (often being so low as to be undetectable), an increasing RMS amplitude during the tail of the burst, and a plateau in the frequency drift at, or

Downloaded from https://academic.oup.com/mnras/article/530/4/3974/7657819 by guest on 04 July 2024

very close to, the NS spin frequency (see Bilous & Watts 2019; Li et al. 2022 for some recent examples). Note, however, there are rare cases of downward frequency drifts being observed instead; the most well-studied example of this is the accreting millisecond pulsar XTE J1814-338 (Strohmayer et al. 2003; Watts, Strohmayer & Markwardt 2005; Watts, Patruno & van der Klis 2008). Given the similarities between Type-I X-ray bursts and micronovae (Scaringi et al. 2022b), a micronova analogue to BOs (i.e. micronova oscillations) warrants consideration.

Since BOs are intrinsically linked to the stellar spin frequency, micronova oscillations naturally explain why the changing frequencies seen in Fig. 7 are so close to the spin frequency of the WD. Moreover, localized TNR further explains the increased spin pulsation amplitude after the micronova: the base of the accretion column has been heated by the burning of material, increasing its luminosity. However, we identify two problems with the micronova oscillation hypothesis: (1) BOs typically display simple frequency drifts, while Figs 7 and 8 show somewhat more complicated changes in frequency, (2) it is unclear why pulsations at the WD spin frequency would be *replaced* by pulsations at a higher frequency (instead of both signals being present simultaneously) if the TNR is localized at the base of the accretion column. However, given that the physical mechanism behind BOs is not yet fully understood (e.g. Watts 2012), we cannot discount micronova oscillations.

5.6.2 *An analogue to pulsar glitches?*

A glitch is a sudden spin-up event seen in pulsars (see Zhou et al. 2022 for a review). There are numerous explanations for pulsar glitches, but the one that is most pertinent to WDs is the starquake theory (e.g. Ruderman 1969; Baym & Pines 1971; Malheiro, Rueda & Ruffini 2012). Within the starquake paradigm, strain builds up in the NS's crust as its liquid core spins down. Inevitably, this strain becomes so large that it reaches a breaking point, resulting in a starquake; this, in turn, results in a rearrangement of the NS's moment of inertia, causing a sudden spin-up (i.e. a 'glitch'). Following a glitch, NSs have often been observed to show an increased spin-down rate (e.g. Zhou et al. 2022).

WD analogues to pulsar glitches have been observed previously (e.g. Malheiro et al. 2012), and so this explanation warrants consideration. However, the multiple frequencies shown in the early epochs of Fig. 7 are difficult to reconcile within the glitch framework. Moreover, it is not clear how the WD would spin back down so quickly, nor is it clear why it would settle back to its pre-burst spin frequency. We also note that the burst's shape (Fig. 3) and subsequent increase in spin pulsation amplitude (Section 5.5.2) are difficult to interpret within this paradigm. For these reasons, we find a WD glitch to be unlikely.

5.7 A change in frequency due to a dwarf nova outburst?

In Section 5.6, we attempted to interpret the apparent change in the WD spin frequency during the burst (Figs 6–8) within the context of a micronova, making analogies to LMXBs. We noted that an analogue to BOs may explain the observed changes in the spin pulsations. However, we also acknowledged that the mechanism behind BOs is not fully understood (e.g. Watts 2012), and so we did not arrive at any confident conclusions. Below, we consider the frequency change within the context of a DN outburst.

5.7.1 *Dwarf nova oscillations?*

It is instructive to note that periodicities are commonly observed during DN outbursts (see Warner 2004 for a review). These periodicities, referred to as DN oscillations (DNOs), typically have periods of up to a few minutes that can vary on time-scales of hours. Because of the varying stabilities of these oscillations, they are typically attributed to some phenomenon in the accretion disc rather than the intrinsic spin of the WD (though there is presently no accepted model of DNOs).

We find DNOs an unlikely explanation for the changing frequencies seen in Fig. 7 since the periods are much longer than typical DNOs. That said, we note that if DNOs originate in the disc, then our results may be suggestive of a highly truncated disc. Alternatively, our longer period may be an alias of a high-frequency DNO. Greiveldinger et al. (2023) speculated that the 29.34-min oscillation they observed during a super-outburst of V844 Her was an alias of a high-frequency DNO, though they concluded that this was unlikely. In our case, it would be highly coincidental for an alias to appear so close to the spin frequency of the WD. For these reasons, we find DNOs to be an unlikely explanation for the frequency drift seen in Figs 6–8.

5.7.2 *An inhomogeneity in the disc?*

If, during a DN outburst, accretion is no longer confined on to the poles (e.g. Hameury & Lasota 2017), then we would not expect to see pulsations at the WD spin frequency. The frequencies seen in the early epochs of Fig. 7 may therefore be pulsations due to some inhomogeneity in the disc slightly below the co-rotation radius ($0.274R_{\odot}$). Assuming a $1.2\,\mathrm{M}_{\odot}$ primary (Bernardini et al. 2017), a Keplerian frequency of $68.35\,\mathrm{d}^{-1}$ corresponds to an orbital radius of $0.268R_{\odot}$. The presence of more than one prominent feature in the early epochs of Fig. 7 may be suggestive of more than one inhomogeneity in the disc at different radii, or an elliptical disc.

In addition to explaining the high-frequency signal, the above interpretation can naturally explain the frequency drift seen in Figs 7 and 8: As accretion begins being channelled back on to the poles, the orbital frequency of the inhomogeneity will increase as it spirals towards the surface. However, the magnetic field of the WD will act to slow the orbital frequency of the infalling material to match its spin frequency. Therefore, the initial increase in orbital frequency will be followed by a decrease down to the spin frequency of the primary, as shown in Figs 7 and 8.

However, it is coincidental that inhomogeneities in the disc would appear so close to the co-rotation radius, unless this is also similar to the magnetospheric/truncation radius. Estimating the magnetospheric radius is non-trivial unless the magnetic moment of the WD is known. Fortunately, the circularization radius defines the upper limit of the magnetospehric radius, and this can be estimated using only the masses and orbital period of the system:

$$r_{\mathrm{circ}} = 3.03 \times 10^{9} q^{-0.426} (M_1 + M_2)^{1/3} P_{\mathrm{orb}}^{2/3}\ \mathrm{cm}, \tag{10}$$

where $q = M_2/M_1$, M_1 is the mass of the WD (in solar masses), M_2 is the mass of the companion (in solar masses), and P_{orb} is the orbital period (in hours; Hameury & Lasota 2017). The circularization radius is the radius at which material would form a circular orbit with the angular momentum it had when leaving the Lagrangian point. As such, the magnetospheric radius *cannot* be larger than the circularization radius. Using $M_1 = 1.2\,\mathrm{M}_{\odot}$ (Bernardini et al. 2017), and the orbital period from Section 5.2.1 (5.9 h), we can yield a circularization radius of $0.27R_{\odot}$, provided the mass of the secondary is $0.4\,\mathrm{M}_{\odot}$. We therefore find it possible that the truncation radius

Downloaded from https://academic.oup.com/mnras/article/530/4/3974/7657819 by guest on 04 July 2024

could be similar to the co-rotation radius, noting that a companion mass of 0.4 $M_\odot$ is not surprising for a CV with an orbital period of ∼6 h (e.g. Knigge et al. 2011).

To check the validity of the above interpretation, we can relate the dynamical and viscous time-scales:

$$\tau_{\rm dyn}(R) \sim \alpha \left(\frac{H}{R}\right)^2 \tau_{\rm visc}(R), \tag{11}$$

where $\tau_{\rm dyn}(R)$ is the dynamical time-scale, α is the disc viscosity, H is the disc thickness, R is the radius, and $\tau_{\rm visc}(R)$ is the viscous time-scale (Shakura & Sunyaev 1973; page 113 of Frank, King & Raine 2002). While we cannot estimate α and H with the available data, we can re-arrange this equation to check that we get a physical value for $\alpha\left(\frac{H}{R}\right)^2$. Shakura & Sunyaev (1973) showed that $\alpha \lesssim 1$, and, if we make the common assumption of a thin disc (e.g. Frank et al. 2002), we also know that $\left(\frac{H}{R}\right)^2 \ll 1$. Assuming $\alpha\left(\frac{H}{R}\right)^2$ is approximately constant throughout the disc, we can write:

$$\alpha\left(\frac{H}{R}\right)^2 = \frac{\tau_{\rm dyn}(R_{\rm co-rotation}) - \tau_{\rm dyn}(R_{\rm WD})}{\tau_{\rm visc}(R_{\rm co-rotation}) - \tau_{\rm visc}(R_{\rm WD})}, \tag{12}$$

where $R_{\rm co\text{-}rotation}$ and $R_{\rm WD}$ are the co-rotation and WD radii, respectively. From Figs 7 and 8, it is clear that the change in viscous time-scales, $\tau_{\rm visc}(R_{\rm co\text{-}rotation}) - \tau_{\rm visc}(R_{\rm WD})$, for an inhomogeneity moving from $R_{\rm co\text{-}rotation}$ to $R_{\rm WD}$ is approximately 1 d. Then using Kepler's third law to compute $\tau_{\rm dyn}(R_{\rm co\text{-}rotation})$ and $\tau_{\rm dyn}(R_{\rm WD})$, we find $\alpha\left(\frac{H}{R}\right)^2 = 0.015$. This satisfies $\alpha \lesssim 1$ and $\left(\frac{H}{R}\right)^2 \ll 1$, and so we conclude that the above explanation is physically justified. However, the above interpretation relies on several coincidences, and so we find it unlikely.

5.7.3 *Partial magnetic confinement?*

The excess of power in the early epochs of Fig. 7 around the spin frequency of the WD suggests some magnetic confinement is still occurring. Assuming partial magnetic confinement onto the poles, the higher frequency signals shown in Figs 7 and 8 may be due to interactions between the Keplerian frequency at the inner-edge of the disc and the magnetic field of the WD. As mentioned in Section 5.7.2, the co-rotation radius is $0.274R_\odot$, meaning any material orbiting below this radius will orbit faster than the WD spin frequency. However, because the WD is magnetized, its magnetic field will act to slow the orbiting material to match its spin frequency (thereby allowing the material to be channelled on to the poles).

If accretion pressure is high (which it is during a DN outburst; Hameury & Lasota 2017), it is plausible that the WD magnetic field may not be sufficiently strong to channel all of the infalling material on to the poles. If enough material is able to overwhelm magnetic confinement, pulsations above the spin frequency of the WD may be observed (since the Keplerian frequency at the WD surface is larger than its spin frequency, causing the accretion column to move across the stellar surface). This interpretation also explains the multiple frequencies shown in the early epochs of Fig. 7: not all of the infalling material will experience the same degree of partial confinement, and so the accretion column may split into two (or more) columns. After roughly 2 d, the accretion pressure becomes sufficiently low for magnetic confinement to dominate again, and accretion is (mostly) confined on to the poles. We acknowledge, however, that the large burst energy found in Section 5.3 is difficult to reconcile within the DN outburst framework, and so this interpretation is not without its challenges.

6 CONCLUSIONS

Using the *TESS* Sector 8 light curve, covering 2019 February 2–27 at 2-min cadence, as well as all available ASAS-SN photometric data, we have conducted a study of the timing properties of bursts in the accreting, mildly magnetic WD PBC J0801.2–4625. In particular, we have analysed this system's February 2019 burst, which was observed simultaneously by ASAS-SN and *TESS*. We found that the burst was best described using a double-peaked shape with a rise time of ≤0.5 d, peak amplitude of ∼2 mag, and duration of ∼2 d. We used the geometric distance of 1355 ± 42 pc from this system's *Gaia* parallax to infer a burst energy lower limit of 3.3×10^{39} erg. The long-term ASAS-SN light curve also showed that this system appears to exhibit bursts with similar peak amplitudes and durations at least every ∼ 1–2 yr. We considered micronovae and DN outbursts to explain this burst, and concluded that it appeared most consistent with a micronova.

Using the high-cadence *TESS* data, we showed that the power spectrum features around the spin frequency of the white dwarf changed significantly during the February 2019 burst. Before and after the burst, power spectra show prominent features at the spin frequency of the WD (66.08 d^{-1}; Bernardini et al. 2017; Halpern et al. 2018). During the burst, however, the most prominent feature in the power spectrum is as high as 68.35 ± 0.28 d^{-1}, with a reduced peak power. We also showed that the RMS amplitude of the spin pulsations before and after the burst increases by a factor 1.82 ± 0.05. After concluding that the burst was most likely a micronova, we suggested that the changes in the spin pulsations could be an analogue to Type I X-ray BOs (i.e. 'micronova oscillations'). However, we also noted that changes in accretion pressure and the amount of magnetic confinement during the burst provide an alternative explanation (implying a DN outburst, in contrast to our conclusion for the burst mechanism). Finally, we note that we found a periodicity in the *TESS* light curve at 5.906 ± 0.003 h that we interpret as the orbital period of this system.

To follow-up this work, high-cadence monitoring of PBC J0801.2–4625 (e.g. using OPTICAM, Castro et al. 2019, or ULTRACAM, Dhillon et al. 2007) is critical. This system has been observed by *TESS* in three sectors, but only exhibited a burst in one. A high-cadence observation that fully covers a future burst would allow for better understanding of the underlying burst mechanism. In particular, detecting a precursor may help to distinguish between micronovae and DN outbursts (see, for example, ASASSN-19bh in Scaringi et al. 2022b). Furthermore, multiwavelength/spectroscopic observations would be especially revealing. Finally, we suggest further searches for changes in the spin pulsations of CVs (both magnetic and non-magnetic) during bursts to better understand the physical process responsible for the changes found in this work.

ACKNOWLEDGEMENTS

This paper includes data collected with the TESS mission, obtained from the MAST data archive at the Space Telescope Science Institute (STScI). Funding for the TESS mission is provided by the NASA Explorer Program. STScI is operated by the Association of Universities for Research in Astronomy, Inc., under NASA contract NAS 5–26555. We gratefully acknowledge use of data provided by the ASAS-SN collaborations.

ZAI acknowledges support from the UK Research and Innovation's Science and Technology Facilities Council (STFC) grant ST/X508767/1. SS is supported by STFC grant ST/X001075/1. NCS acknowledges support by STFC grants ST/V001000/1 and

Downloaded from https://academic.oup.com/mnras/article/530/4/3974/7657819 by guest on 04 July 2024

ST/X001121/1. KI was supported by Polish National Science Center grant Sonatina 2021/40/C/ST9/00186. MV acknowledges the support of the STFC studentship ST/W507428/1. DDM acknowledges financial support from INAF Astrofund-2022 project 'FANS'.

We thank Andrés Gúrpide for informative discussions, and Anwesha Sahu for helpful suggestions. We also thank the anonymous referee for helpful suggestions that have improved the paper.

This research also made use of ASTROPY,[8] (Astropy Collaboration 2013, 2018); Lightkurve (Lightkurve Collaboration 2018); MATPLOTLIB (Hunter 2007); NUMPY (Harris et al. 2020); SCIPY (Virtanen et al. 2020); and ULTRANEST (Buchner 2021).

DATA AVAILABILITY

All data analysed herein are publicly available via the ASAS-SN light-curve server,[9] and the Mikulski Space Archive for Space Telescopes (MAST): doi:10.17909/draq-b740.

REFERENCES

Allan A., Hellier C., Ramseyer T. F., 1996, MNRAS, 282, 699
Angelini L., Verbunt F., 1989, MNRAS, 238, 697
Astropy Collaboration, 2013, A&A, 558, A33
Astropy Collaboration, 2018, AJ, 156, 123
Baym G., Pines D., 1971, Ann. Phys., 66, 816
Bernardini F., de Martino D., Mukai K., Russell D. M., Falanga M., Masetti N., Ferrigno C., Israel G., 2017, MNRAS, 470, 4815
Bhattacharyya S., Strohmayer T. E., 2006a, ApJ, 636, L121
Bhattacharyya S., Strohmayer T. E., 2006b, ApJ, 641, L53
Bilous A. V., Watts A. L., 2019, ApJS, 245, 19
Buchner J., 2016, Stat. Comput., 26, 383
Buchner J., 2019, Publ. Astron. Soc. Pac., 131, 108005
Buchner J., 2021, J. Open Source Softw., 6, 3001
Buchner J., 2022, Phys. Sci. Forum, 5, 46
Buchner J. et al., 2014, A&A, 564, A125
Buckley D. A. H., Tuohy I. R., 1989, ApJ, 344, 376
Buckley D. A. H. et al., 1995, MNRAS, 275, 1028
Buckley D. A. H., Haberl F., Motch C., Pollard K., Schwarzenberg-Czerny A., Sekiguchi K., 1997, MNRAS, 287, 117
Bult P. et al., 2019, ApJ, 885, L1
Castro A. et al., 2019, Rev. Mex. Astron. Astrofis., 55, 363
Cumming A., Marcy G. W., Butler R. P., 1999, ApJ, 526, 890
Dhillon V. S. et al., 2007, MNRAS, 378, 825
Frank J., King A., Raine D. J., 2002, Accretion Power in Astrophysics: Third Edition, Cambridge University Press.
Galloway D. K., Muno M. P., Hartman J. M., Psaltis D., Chakrabarty D., 2008, ApJS, 179, 360
Greiveldinger A. et al., 2023, ApJ, 955, 150
Halpern J. P., Thorstensen J. R., Cho P., Collver G., Motsoaledi M., Breytenbach H., Buckley D. A. H., Woudt P. A., 2018, AJ, 155, 247
Hameury J. M., Lasota J. P., 2017, A&A, 602, A102
Hameury J. M., Lasota J. P., 2021, A&A, 650, A114
Harris C. R. et al., 2020, Nature, 585, 357
Hellier C., 1991, MNRAS, 251, 693
Hellier C., Beardmore A. P., 2002, MNRAS, 331, 407
Hellier C., Garlick M. A.,Mason K. O. , 1993, MNRAS, 260, 299
Hellier C. et al., 2000, MNRAS, 313, 703
Hunter J. D., 2007, Comput. Sci. Eng., 9, 90
Iłkiewicz K. et al., 2024, ApJ, 962, L34
Jaisawal G. K. et al., 2019, ApJ, 883, 61
Kato T., 2015, Publ. Astron. Soc. Japan, 67, 108
Keek L., Heger A., 2017, ApJ, 842, 113
Knigge C., Baraffe I., Patterson J., 2011, ApJS, 194, 28
Kochanek C. S. et al., 2017, Publ. Astron. Soc. Pac., 129, 104502
Lasota J.-P., 2001, New Astron Rev., 45, 449
Li Z., Yu W., Lu Y., Pan Y., Falanga M., 2022, ApJ, 935, 123
Lightkurve Collaboration, 2018, Astrophysics Source Code Library, record ascl:1812.013.
Lomb N. R., 1976, Ap&SS, 39, 447
Malheiro M., Rueda J. A., Ruffini R., 2012, Publ. Astron. Soc. Japan, 64, 56
O'Donoghue D., Koen C., Kilkenny D., 1996, MNRAS, 278, 1075
Parker T. L., Norton A. J., Mukai K., 2005, A&A, 439, 213
Patterson J., 1981, ApJS, 45, 517
Rawat N., Pandey J. C., Joshi A., 2021, ApJ, 912, 78
Reimer T. W., Welsh W. F., Mukai K., Ringwald F. A., 2008, ApJ, 678, 376
Retter A., Leibowitz E. M., Kovo-Kariti O., 1998, MNRAS, 293, 145
Ruderman M., 1969, Nature, 223, 597
Scargle J. D., 1982, ApJ, 263, 835
Scaringi S. et al., 2022a, MNRAS, 514, L11
Scaringi S. et al., 2022b, Nature, 604, 447
Shakura N. I., Sunyaev R. A., 1973, A&A, 24, 337
Shappee B. J. et al., 2014, ApJ, 788, 48
Skilling J., 2004, in Fischer R., Preuss R., Toussaint U. V.eds, AIP Conf. Ser. Vol. 735, Bayesian Inference and Maximum Entropy Methods in Science and Engineering: 24th International Workshop on Bayesian Inference and Maximum Entropy Methods in Science and Engineering. Am. Inst. Phys., New York. p. 395
Skilling J., 2009, in Goggans P. M., Chan C.-Y.eds, AIP Conf. Ser. Vol. 1193, Bayesian Inference and Maximum Entropy Methods in Science and Engineering: The 29th International Workshop on Bayesian Inference and Maximum Entropy Methods in Science and Engineering. Am. Inst. Phys., New York. p. 277
Strohmayer T. E., Markwardt C. B., Swank J. H., in't Zand J., 2003, ApJ, 596, L67
Thorstensen J. R., 1997, Publ. Astron. Soc. Pac., 109, 1241
VanderPlas J. T., 2018, ApJS, 236, 16
VanderPlas J. T., Ivezić Ž., 2015, ApJ, 812, 18
Veresvarska M. et al., 2024, MNRAS, 529, 664
Virtanen P. et al., 2020, Nat. Methods, 17, 261
Warner B., 1995, Cataclysmic Variable Stars. Vol. 28, Cambridge University Press.
Warner B., 2004, Publ. Astron. Soc. Pac., 116, 115
Watts A. L., 2012, ARA&A, 50, 609
Watts A. L., Strohmayer T. E., Markwardt C. B., 2005, ApJ, 634, 547
Watts A. L., Patruno A., van der Klis M., 2008, ApJ, 688, L37
Zemko P., Orio M., Luna G. J. M., Mukai K., Evans P. A., Bianchini A., 2017, MNRAS, 469, 476
Zhou S., Gügercinoğlu E., Yuan J., Ge M., Yu C., 2022, Universe, 8, 641
Zurek D. R., Knigge C., Maccarone T. J., Dieball A., Long K. S., 2009, ApJ, 699, 1113

This paper has been typeset from a TEX/LATEX file prepared by the author.

[8] http://www.astropy.org
[9] https://asas-sn.osu.edu

© The Author(s) 2024.
Published by Oxford University Press on behalf of Royal Astronomical Society. This is an Open Access article distributed under the terms of the Creative Commons Attribution-NonCommercial License (http://creativecommons.org/licenses/by-nc/4.0/), which permits non-commercial re-use, distribution, and reproduction in any medium, provided the original work is properly cited.

Downloaded from https://academic.oup.com/mnras/article/530/4/3974/7657819 by guest on 04 July 2024